journal

Ni-Ti Codoped Hibonite Ceramic Pigments by Combustion Synthesis: Crystal Structure and Optical Properties

Matteo Ardit,[‡,†] Silvana Borcănescu,[§] Giuseppe Cruciani,[‡] Michele Dondi,[¶] Ioan Lazău,[§] Cornelia Păcurariu,[§] and Chiara Zanelli[¶]

[‡]Department of Physics and Earth Sciences, University of Ferrara, Ferrara, Italy

[§]Faculty of Industrial Chemistry and Environmental Engineering, Politehnica University of Timişoara, Timişoara, Romania

[¶]CNR-ISTEC, Institute of Science and Technology for Ceramics, Faenza, Italy

Hibonite ($CaAl_{12}O_{19}$, space group [s.g.] $P6_3/mmc$) has the structural formula $A^{[XII]}M1^{[VI]}\ M2^{[V]}M3_2^{[IIV]}M4_2^{[VI]}M5_6^{[VI]}O_{19}$, where Ca is 12-fold coordinated at site A and Al^{3+} ions are distributed over five different sites: three distinct octahedra [M1 (point symmetry D_{3d}), M4 (C_{3v}) and M5 (C_s)], the M3 tetrahedron (C_{3v}), and the unusual fivefold coordinated trigonal bipyramid M2 (D_{3h}). Hibonite is able to accommodate a wide range of ions with different valence and coordination, making its structure a promising ceramic pigment. One of the main challenges is to understand and control incorporation mechanisms and the threshold of chromophores solubility. It is known that M^{2+} ions tend to be hosted at the M3 site, while M^{4+} ions are preferentially accommodated at the M4 site: the introduction of divalent ions might be promoted by the associated incorporation of tetravalent cations, which ensure the lattice electroneutrality and are ordered over the M4 face-sharing octahedral dimers. In this work, the mechanism of the coupled substitution $2Al^{3+} \rightarrow (Ni^{2+}+Ti^{4+})$ was investigated by combining X-ray powder diffraction and diffuse reflectance spectroscopy techniques. Hibonite turquoise pigments with increasing Ni+Ti doping ($CaAl_{12\ 2x}Ni_xTi_xO_{19}$ where $x = 0.1$ 2.0 apfu) were prepared by combustion synthesis, utilizing a fuel mixture (urea, glycine, β-alanine) set up according to their compatibility with metal nitrates used as raw materials. The ignition temperature of combustion reaction was 400°C, but samples underwent an additional annealing at 1200°C. Samples up to $x = 0.4$ are monophasic; for higher doping, hibonite is the main component accompanied by growing percentages of spinel and perovskite phases. The Ni and Ti addition induced a regular increase in the hibonite unit-cell parameters until $x = 1.0$, that is proportional to the amount and difference in ionic radii of dopants. In particular, an elongation of the ⟨M–O⟩ bond distances of both M3 and M4 sites was observed. In terms of optical parameters, Ni^{2+} is preferentially incorporated in tetrahedral coordination, up to 0.3 apfu at the M3 site, and at the M4 octahedron as well (up to 0.19 apfu). The crystal field strength of fourfold coordinated Ni^{2+} is regularly decreasing, implying an elongation of the local Ni-O bond that is coherent with the volume increasing from AlO_4 to NiO_4 tetrahedra registered by XRD. Ti^{4+} ions are accommodated at both the M2 and M4 octahedra which expand proportionally to the amount of dopants. Pigment purity and color strength vary with doping depending on the multistep mechanism of Ni and Ti incorporation in the hibonite lattice.

J. McKittrick—contributing editor

I. Introduction

THE development of new pigments requires an accurate design of several factors related with the origin of color, including the knowledge of valence state and ligand environment of the ion responsible for coloration (hereafter called *chromophore*).[1,2] In particular, colors based on the crystal field theory strongly depend on valence and coordination of the chromophore,[3] especially when it is a dopant inside a crystal structure for which main component is not a transition-metal ion. From this standpoint, the chromophore accommodation at polyhedral sites of the crystal structure plays a key role, making local metal oxygen distances, site distortion, and degree of occupancy by one or more ions as fundamental parameters for color development.[2–4] Along with the chromophore, a second dopant is often added, in the case of a heterovalent substitution, to ensure the electrostatic neutrality of the crystal lattice (called codopant).

The design of new pigments is simpler for crystal structures having a single cationic site, e.g., corundum[5,6] or rutile,[7,8] circumstance that prevents order–disorder phenomena in the partition of dopant and main component. Similarly, the control is easier for crystalline phases which exhibit two polyhedra with distinct volume and coordination number, and therefore host cations with different radii and valence states, as in the case of the cubic and octahedral sites of perovskite,[9,10] or the cubic and tetrahedral sites of zircon.[11,12] However, the pigment design turns to be challenging as far as complex structures are concerned, i.e., those where three or more cationic sites are present, particularly if ions partition over different polyhedra can occur. Typical examples are phases with high thermal and chemical stability, hence good candidates for ceramic pigments, like zirconolite,[13,14] or murataite,[15,16] whose complex crystal chemistry makes their development problematic.

This picture, further complicated by the competition of different cations to be accommodated at the same site (main component, chromophore, and a possible codopant), can explain why successful ceramic pigments are restricted to a limited number of structures, in most cases with only one or two cationic sites.[1,2] The most complex crystal structures used as ceramic pigments have three well-distinct cationic sites and suffer from remarkable problems in the synthesis control, i.e., garnet[17,18] and malayaite.[19,20] Nevertheless, a better knowledge of mechanisms governing the competition of cations for different polyhedra and of the order/disorder phenomena should disclose the possibility to improve the design and to obtain better pigments. On the other hand, the large body of literature on crystal/melt equilibria is not directly applicable, because industrial synthesis entails mostly solid-state reactions in nonequilibrium conditions, where kinetic effects are overwhelming.[21,22] This circumstance is

particularly true for hibonite that is notoriously hard to synthesize as pure specimens by solid-state reactions.[23] In order to improve the reaction yield of the conventional solid-state route, a combustion synthesis was adopted in the present work.

Hibonite ($CaO \cdot 6Al_2O_3$) represents an ideal material to verify how the main component, chromophore and codopant compete for the access to different polyhedra. In fact, its crystal structure, being isostructural with the magnetoplumbite-type structure (s.g. $P6_3/mmc$, $Z = 2$), presents the following general crystal chemical formula:[24,25]

$$A^{[XII]}M1^{[VI]}M2_2^{[V]}M3_2^{[IV]}M4_2^{[VI]}M5_6^{[VI]}O_{19}$$
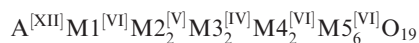
with considerable variation in its chemical composition. Calcium cations occur in 12-fold coordination (site A), whereas the Al^{3+} ions are distributed over five different coordination sites, including three distinct octahedra [M1 (point symmetry D_{3d}), M4 (C_{3v}), and M5 (C_s)], the M3 tetrahedron (C_{3v}), as well as an unusual trigonal bipyramid [M2 (D_{3h})] fivefold coordinated by oxygen ions.[26–28] The polyhedral arrangement in the hibonite structure is depicted in Fig. 1. It can be schematized as a repetition of two distinct and alternated polyhedral layers parallel to (001).[3] Specifically, the tetrahedral (M3) and octahedral (M1 and M5) polyhedra are located in the so-called spinel block ($S = [M_6O_8]^{2+}$), whereas the Ca site and the trigonal bipyramidal M2 and the octahedral M4 polyhedra are located in a hexagonal close-packed block ($R = [CaM_6O_{11}]^{2-}$). The entire hibonite unit cell is composed by a staking of R- and S-blocks along the *c*-axis in a S′RSR′S′ sequence, where R′ and S′ are blocks rotated by 180° about the *c*-axis relative to R and S, respectively.[27]

In natural hibonites, it is known that M^{2+} ions tend to be hosted at the M3 tetrahedral site, while M^{4+} and M^{5+} ions are preferentially accommodated at the M4 octahedral site.[27,29] The preference of divalent cations (e.g., Mg^{2+}, Fe^{2+}, Zn^{2+}, Ni^{2+}) for the M3 site of magnetoplumbite group minerals has been found also in several synthetic compounds. This is possible because these substitutions are electrostatically more favorable than the incorporation of highly charged cations, as it has been demonstrated by consideration of Pauling bond-strength sums,[24] Bond valence sum ($BVsum$),[30] and by calculation of the Madelung factors for various hypothetical schemes of cation distribution.[25] As far as Ni^{2+} is concerned, its strong preference for the tetrahedral

site still holds in spite of its larger crystal field stabilization energy (CFSE) for the octahedral coordination.[27]

Guidelines in pigment design are usually ionic radius, valence, and coordination, which can be integrated by the CFSE.[3] Further parameters, like the $BVsum$,[31,32] have been claimed to account for deviation from general rules, as in melilite and perovskite.[31,33] These aspects were investigated in natural hibonites,[24,27–29] but pigment synthesis widen the perimeter of possible dopants, their concentration, and association as in the case of Ni- and Ti-doped hibonite. The Al^{3+} partial substitution is facilitated by a coupled substitution, where $Ni^{2+}+Ti^{4+}$ replace two Al^{3+} ions. Ni-doped hibonite was discovered by Costa et al. (2009) who utilized tin as codopant.[34] Titanium was used as codopant of cobalt in hibonite pigment by Leite et al. (2010) and Dondi et al. (2014).[31,35]
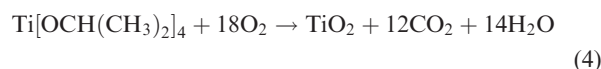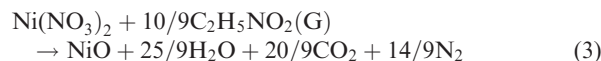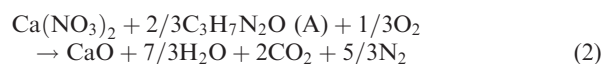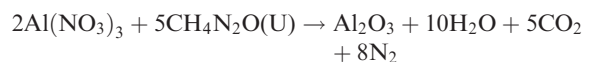
An investigation was here undertaken to understand in depth the behavior of Ni and Ti ions, added as dopants to an ideal hibonite formulation (as a test bench) in increasing concentration, by a combined X-ray diffraction and optical spectroscopy approach.

II. Experimental Procedure

(1) Synthesis

The hibonite samples were prepared by the combustion synthesis method based on highly exothermic redox reactions between solid fuels and metal nitrates. Such a procedure was used for the synthesis of different thermoresistant pigments.[36–38] The following reagents were used: $Ca(NO_3)_2 \cdot 4H_2O$ (Merck), $Al(NO_3)_2 \cdot 9H_2O$ (Merck), $Ni(NO_3)_2 \cdot 6H_2O$ (Merck), titanium isopropoxide $Ti[OCH(CH_3)_2]_4$ (Reactivul), urea CH_4N_2O (Merck), β-alanine $C_3H_7NO_2$ (Merck), and glycine $C_2H_5NO_2$ (Fluka).

Previous results have proved the existence of a variable degree of compatibility between the nitrate nature (oxidizing) and the organic/fuel nature (reducing) and thus, the need for a rational choice of fuel mixtures for maximizing the chances of obtaining the designed oxide compounds directly from the combustion synthesis.[39–44] The compatibility between the nature of the metal nitrate and fuel was established on the basis of thermal analyses and on the phase composition determination in the case of preparation of calcium aluminates.[36,37,40] Based on these results, urea (CH_4N_2O) was chosen as related fuel for aluminum nitrate, β-alanine ($C_3H_7NO_2$) for calcium nitrate, and glycine ($C_2H_5NO_2$) for nickel nitrate. The reagents dosage was designed starting from the following premise: oxidation–reduction processes must be completed, the reaction products are the desired oxide compounds, and CO_2, H_2O, and N_2 are secondary reaction products. For exemplification, the general reactions between aluminum nitrate and urea (U), calcium nitrate and β-alanine (A), and nickel nitrate and glycine (G) are presented as follows:

$$2Al(NO_3)_3 + 5CH_4N_2O(U) \rightarrow Al_2O_3 + 10H_2O + 5CO_2 + 8N_2$$

$$(1)$$

$$Ca(NO_3)_2 + 2/3C_3H_7N_2O\ (A) + 1/3O_2 \rightarrow CaO + 7/3H_2O + 2CO_2 + 5/3N_2$$

$$(2)$$

$$Ni(NO_3)_2 + 10/9C_2H_5NO_2(G) \rightarrow NiO + 25/9H_2O + 20/9CO_2 + 14/9N_2$$

$$(3)$$

$$Ti[OCH(CH_3)_2]_4 + 18O_2 \rightarrow TiO_2 + 12CO_2 + 14H_2O$$

$$(4)$$

Eight samples were designed according to the general formula: $CaAl_{12-2x}Ni_xTi_xO_{19}$, where x: 0.1, 0.2, 0.3, 0.4, 0.5, 1.0, 1.5, and 2.0 apfu (see Table SI).
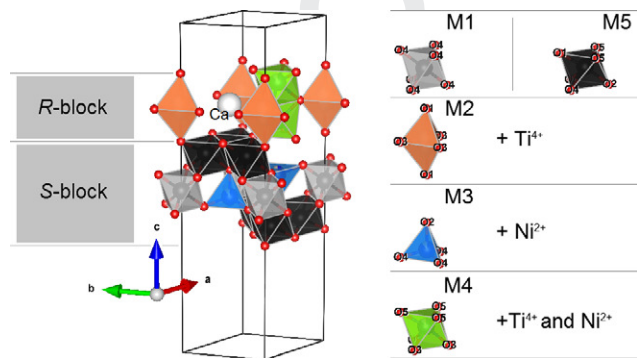

Fig. 1. Polyhedral representation of the two structural layers, *R*-block (i.e., the Ca site, the trigonal bipyramidal M2 site, and the octahedral face-sharing M4 site) and *S*-block (i.e., layers of M5 octahedra interspaced by the M3 tetrahedra and the M1 octahedra) of Ni and Ti codoped hibonite (s.g. $P6_3/mmc$) in a perspective as view along [110]. The atom of Ca (a white sphere) is 12-fold coordinated by $6 \times O3$ and $6 \times O5$. On the right side, a representation of each polyhedron with their respective ligands and the occupancy of the dopants (i.e., Ni^{2+} and Ti^{4+}; for further details see next sections). Figure obtained by means of the VESTA v.3.2.1 visualizer.[69]

Amounts of reagents were calculated for obtaining 0.015 moles of $CaAl_{12}O_{19}$. The dissolution of the desired metal nitrates together with the appropriate amounts of fuels was conducted in porcelain vessels in a minimum amount of distilled water. Afterward, the mixtures have been subjected to partial evaporation in the drying stove at 50°C followed by a initiation process of oxidation–reduction in a preheated kiln at 400°C with SiC as heating element to initiate the combustion reaction. The high temperature reached within the raw material mixture led to the formation of a blue-colored, dried fluffy foam, which was easily deagglomerated into a fine powder. The time of combustion for the synthesis development varied from 40 to 46 s. The resulting powders were then annealed in an electric furnace at a temperature of 1200°C with 1 h soaking time.

(2) X-ray Powder Diffraction Data Collection and Rietveld Refinements

X-ray powder diffraction measurements were performed at room temperature using a Bruker D8 Advance Diffractometer on a Bragg-Brentano geometry with an X-ray tube operating at 40 kV and 40 mA. Data were collected through a one-dimensional LynxEye detector based on silicon strip technology, set to discriminate $CuK_{\alpha 1,2}$ radiation in the 10°–130°2θ measuring range, with an equivalent counting time of 16 s per 0.02°2θ step.

Structural parameters were determined from whole pattern profile fitting of the diffraction data by the Rietveld method using the GSAS code implemented into the EXPGUI interface.[45,46]

The presence of associated phases, detected in small concentrations for samples with a nominal amount of Ni+Ti = 1 and 2 apfu (i.e., for samples 5 and 10; see Table I), was accounted for by carrying out multiphase refinements in which only the scale factors and the cell parameters were varied, except for the hibonite main phase. The starting structural models employed during the Rietveld refinement were those of Nagashima et al. (for the hibonite structure, hexagonal s.g. $P6_3/mmc$),[30] O'Neill et al. (for the spinel structure, cubic s.g. $Fd–3m$),[47] Sasaki et al. (for the perovskite structure, orthorhombic s.g. $Pbnm$),[48] and Cherginets et al. (for the corundum structure, trigonal s.g. $R–3c$).[49]

Peak profiles were modeled by a pseudo-Voigt function, with the peak cut-off set to 0.05% of the peak maximum, by means of the θ-independent Gaussian (GW) and the two $(\cos θ)^{-1}$- and $(\tan θ)$-dependent Lorentzian (i.e., LX, and LY, respectively) broadening coefficients plus an asymmetry contribution. Besides 18 shifted Chebyshev polynomial coefficients to reproduce the background, the refinements included a scale factor, cell parameters (a- and c-axis), atomic coordinates (x, y, z), and isotropic atomic displacement parameters, ADPs (U_{iso}).

Agreement factors and refinement details are listed in Table I. Unit-cell parameters, site occupancy, and selected metal–oxygen bond distances of the hibonite structure for samples along the $CaNi_xTi_xAl_{12-2x}O_{19}$ join are summarized in Table I and II.

It is noteworthy that Ni and Ti were initially included in the refinement based on the nominal stoichiometry, and then varied as required by the refinement process. Specifically, both cations were iteratively placed at each M site (i.e., M1, M4, and M5 octahedra, M3 tetrahedron, and M2 trigonal bipyramid) so that all the different cationic coordinations were checked. All cationic distribution models different from that reported in Table II lead to a divergence of Rietveld refinements or to unphysical structural parameters.

Due to the nonreducing synthesis conditions (the combustion process took place in air), the titanium cation has been considered as fully oxidized (i.e., as Ti^{4+}). It follows that, in order to maintain the hibonite structure electrostatically neutral, the nickel cation has been considered as bivalent (i.e.,

Ni^{2+}). This latter assumption was corroborated both by convergence of Rietveld refinements of XRPD patterns, and through deconvolution of optical spectra (see next sections).

Ni^{2+} and Ti^{4+} site occupancies were kept as fixed during the least-squares refinements and manually iterated between refinement cycles. Due to the high mutual correlations, atomic coordinates, ADPs, and site occupancy were varied in alternate cycles. Cations hosted at the same coordination site (i.e., Al^{3+} and Ti^{4+} at the trigonal bipyramidal M2 site, Al^{3+} and Ni^{2+} at the tetrahedral M3 site, and Al^{3+}, Ni^{2+} and Ti^{4+} at the octahedral M4 site) were constrained to maintain the chemical composition and to change the isotropic temperature factors identically.

(3) Electronic Absorption Spectroscopy

Optical measurements were performed by diffuse reflectance (PerkinElmer λ19 spectrophotometer, 250 2500 nm range, 0.3 nm step size, speed 240 nm/min, $BaSO_4$ integrating sphere, white reference material: $BaSO_4$ pellet). Reflectance (R_∞) was converted to absorbance (K/S) by the Kubelka–Munk equation: $K/S = (1 R_\infty)^2 \cdot (2R_\infty)^{-1}$.[50] Absorbance bands were deconvoluted by a pseudo-Voigt function (PFM, OriginLab) starting from peak maxima by automatic fitting to convergence, in order to obtain the band energy (centroid), width (FWHM), and intensity (peak area) for which experimental errors, including background correction and reproducibility, are within 1%, 3%, and 5%, respectively.

The crystal field strength $10Dq$ was determined by: (1) $10Dq_{oct}$ = octahedrally coordinated Ni^{2+} as the energy of the $^3T_{2g}(^3F)$ transition; (2) $10Dq_{tet}$ = tetrahedrally coordinated Ni^{2+} as the energy difference of $^3A_2(^3F) – ^3T_2(^3F)$ transitions; adopting, for sake of simplicity, the terminology for the cubic symmetry (O_h for the octahedral coordination and T_d for the tetrahedral coordination). Since the $^3T_2(^3F)$ transition of Ni^{2+} in tetrahedral coordination is twice split, due to the effect of both Ni^{2+} spin-orbit coupling and the low point symmetry, its energy was calculated as the mean value of the two sub-bands.

The Racah B parameter was calculated by fitting the spin-allowed transitions of Ni^{2+} ion in the d^8 Tanabe–Sugano diagram (for the octahedral coordination) and in the d^2 diagram that is used, according to the d^{10-N} rule, in the case of ions in fourfold coordination.[51,52]

The relative abundance of tetrahedrally coordinated nickel (Ni^{2+}_{tet}) and octahedrally coordinated nickel (Ni^{2+}_{oct}) was determined by assuming the nominal amount of Ni = (Ni^{2+}_{tet} + Ni^{2+}_{oct}). In order to account for the much higher transition probability of Ni^{2+}_{tet} (one order of magnitude more than Ni^{2+}_{oct}) two transitions with close wave number and similar intensity were selected instead of the most intense bands. By this way the peak area (Γ) of the $^3A(^3F)$ band of Ni^{2+}_{tet} at ~8800 cm^{-1} was made comparable with the peak area of the $^3T_{2g}(^3F)$ band of Ni^{2+}_{oct} at ~9400 cm^{-1}. The relative amount of Ni^{2+}_{tet} was calculated as $\Gamma(^3A)/\Gamma(^3A + ^3T_{2g})$; that of Ni^{2+}_{oct} as $(^3T_{2g})/\Gamma(^3A + ^3T_{2g})$.

III. Result and Discussion

(1) X-ray Diffraction

(A) Quantitative Phase Analyses: Data listed in Table I show that samples 1, 2, 3, and 4 are monophasic with a hibonite structure type. This implies that, by means of our synthesis conditions, the incorporation of Ni and Ti ions into the hibonite structure was fully attained up to a nominal content of Ni+Ti = 0.8 apfu. From sample 5, the amount of the hibonite phase is primarily and proportionally contrasted by the formation of an associated spinel phase (see Table I). For the highest levels of doping, i.e., for those samples characterized by a nominal content of Ni+Ti > 2 apfu, the formation of the hibonite structure seems to be strongly hindered by a reaction kinetics which favors the formation of other

Table I. Quantitative Phase Analysis, Nominal and Recalculated Hibonite Composition, Goodness of Fit (Agreement Factors), and Refinement Details for Samples Belonging to the Series $CaNi_xTi_xAl_{12-2x}O_{19}$ (with $0.1 \leq x \leq 2$)

Sample	1	2	3	4	5	10	15	20
Quantitative phase analysis (wt%)								
Hibonite ($CaAl_{12}O_{19}$)	100	100	100	100	96.3 (1)	91.5 (1)	72.1 (1)	53.1 (1)
Spinel ($NiAl_2O_4$)	–	–	–	–	2.9 (1)	6.5 (1)	24.3 (1)	35.2 (1)
Corundum (Al_2O_3)	–	–	–	–	–	2.0 (1)	–	–
Perovskite ($CaTiO_3$)	–	–	–	–	0.8 (1)	–	3.6 (1)	11.7 (1)
Composition of the $CaMO_{19}$, M:								
Nominal	$Al_{11.8}Ni_{0.1}Ti_{0.1}$	$Al_{11.6}Ni_{0.2}Ti_{0.2}$	$Al_{11.4}Ni_{0.3}Ti_{0.3}$	$Al_{11.2}Ni_{0.4}Ti_{0.4}$	$Al_{11.0}Ni_{0.5}Ti_{0.5}$	$Al_{10.0}Ni_{1.0}Ti_{1.0}$	$Al_{9.0}Ni_{1.5}Ti_{1.5}$	$Al_{8.0}Ni_{2.0}Ti_{2.0}$
Recalculated	$Al_{11.8}Ni_{0.1}Ti_{0.1}$	$Al_{11.6}Ni_{0.2}Ti_{0.2}$	$Al_{11.4}Ni_{0.3}Ti_{0.3}$	$Al_{11.2}Ni_{0.4}Ti_{0.4}$	$Al_{11.0}Ni_{0.5}Ti_{0.5}$	$Al_{10.0}Ni_{0.98}Ti_{1.0}$	$Al_{9.0}Ni_{1.38}Ti_{1.48}$	$Al_{8.0}Ni_{1.77}Ti_{1.92}$
Agreement factors and refinement details								
R_{wp}	0.0699	0.0523	0.0639	0.0487	0.0498	0.0411	–	–
R_p	0.0507	0.0380	0.0454	0.0343	0.0326	0.0284	–	–
No. of data	6080	6080	6080	6080	6080	6080	–	–
No. of variables	38	38	38	38	44	44	–	–
$R(F^2)$	0.0470	0.0466	0.0534	0.0456	0.0544	0.0728	–	–
Hibonite (s.g. P_{63}/mmc)								
No. of reflections	474	474	475	475	475	481	–	–
$R(F)$	0.0281	0.0257	0.0344	0.0297	0.0376	0.0609	–	–
Unit-cell parameters								
$a = b$ (Å)	5.5655 (2)	5.5695 (2)	5.5740 (4)	5.5807 (3)	5.5813 (3)	5.5975 (3)	*5.5987 (2)*	*5.5996 (2)*
c (Å)	21.9276 (9)	21.9433 (6)	21.9555 (15)	21.9830 (10)	21.9892 (13)	22.1002 (11)	*22.1306 (10)*	*22.1473 (15)*
V (Å^3)	588.20 (6)	589.47 (4)	590.75 (10)	592.91 (7)	593.21 (9)	599.68 (8)	*600.79 (7)*	*601.44 (9)*

Data on the recalculated hibonite composition are those obtained by weighting the nominal composition for the amount of the associated phases. In italic, data obtained by a preliminary fit of the powder diffraction patterns through the HIGHSCORE PLUS v3.0 software; no structural investigation has been performed on this data. Furthermore, agreement factors and unit-cell parameters for the hibonite structure. Standard deviations are within parentheses.

Table II. Ni and Ti Site Occupancies (as Fraction of 1) and Selected Interatomic Bond Distances (with their Standard Deviations within Parentheses) Along the Series CaNi$_x$Ti$_x$Al$_{12-2x}$O$_{19}$ (with 0.1 ≤ x ≤ 1)

Sample		1	2	3	4	5	10
[XII]Ca([VI]M1[V]M2[IV]M3$_2$[VI]M4$_2$[VI]M5$_6$)O$_{19}$ *site occupancy* (M1 and M5 fully occupied by Al^{3+})							
M2	Al^{3+}	0.986	0.954	0.850	0.880	0.900	0.260
	Ti^{4+}	0.014	0.046	0.150	0.120	0.100	0.740
M3	Al^{3+}	0.964	0.929	0.902	0.874	0.812	0.694
	Ni^{2+}	0.036	0.071	0.099	0.126	0.188	0.306
M4	Al^{3+}	0.943	0.894	0.874	0.786	0.738	0.676
	Ti^{4+}	0.043	0.077	0.075	0.140	0.200	0.130
	Ni^{2+}	0.014	0.029	0.052	0.074	0.062	0.194
Interatomic bond distances (Å)							
	Ca–O3 (×6)	2.785 (2)	2.787 (2)	2.789 (3)	2.793 (3)	2.794 (3)	2.801 (3)
	Ca–O6 (×6)	2.713 (3)	2.712 (3)	2.709 (5)	2.710 (3)	2.711 (3)	2.690 (4)
Mean	⟨Ca–O⟩	2.749 (3)	2.749 (2)	2.749 (4)	2.752 (3)	2.752 (4)	2.746 (4)
	M1–O4 (×6)	1.881 (3)	1.883 (2)	1.888 (4)	1.884 (3)	1.876 (4)	1.896 (4)
	M2–O1$_a$	2.457 (10)	2.453 (8)	2.487 (13)	2.464 (10)	2.457 (12)	2.574 (12)
	M2–O1$_b$	2.016 (6)	1.992 (5)	1.950 (8)	1.948 (6)	1.944 (8)	1.845 (7)
	M2–O3 (×3)	1.730 (5)	1.741 (4)	1.744 (7)	1.754 (5)	1.759 (6)	1.771 (7)
Mean	[4]⟨M2–O⟩	1.802 (5)	1.804 (4)	1.796 (7)	1.803 (5)	1.805 (6)	1.790 (7)
Mean	[5]⟨M2–O⟩	1.933 (6)	1.934 (5)	1.934 (9)	1.935 (6)	1.936 (8)	1.946 (8)
	M3–O2	1.811 (5)	1.817 (4)	1.822 (6)	1.828 (5)	1.830 (6)	1.873 (6)
	M3–O4 (×3)	1.798 (3)	1.802 (2)	1.802 (4)	1.805 (3)	1.808 (4)	1.817 (4)
Mean	⟨M3–O⟩	1.801 (4)	1.805 (3)	1.807 (5)	1.811 (4)	1.814 (5)	1.831 (5)
	M4–O3 (×3)	1.964 (4)	1.965 (3)	1.967 (5)	1.966 (4)	1.962 (4)	2.015 (5)
	M4–O5 (×3)	1.874 (4)	1.878 (3)	1.876 (5)	1.887 (4)	1.890 (4)	1.885 (5)
Mean	⟨M4–O⟩	1.919 (4)	1.922 (3)	1.922 (5)	1.927 (4)	1.926 (4)	1.950 (5)
	M5–O1	1.838 (3)	1.847 (2)	1.860 (4)	1.861 (3)	1.863 (4)	1.901 (4)
	M5–O2	1.991 (3)	1.994 (3)	1.984 (4)	1.990 (3)	1.992 (4)	1.937 (4)
	M5–O4 (×2)	1.999 (2)	1.994 (2)	1.992 (3)	1.990 (2)	1.992 (4)	1.987 (3)
	M5–O5 (×2)	1.819 (3)	1.819 (4)	1.825 (3)	1.828 (2)	1.827 (3)	1.836 (3)
Mean	⟨M5–O⟩	1.911 (3)	1.911 (2)	1.913 (3)	1.914 (2)	1.916 (3)	1.914 (3)
	M4–M4	2.543 (5)	2.563 (4)	2.557 (7)	2.571 (5)	2.570 (6)	2.692 (6)
	O1–O1 (R)	4.473	4.446	4.437	4.412	4.401	4.419
	O1–O1 (S)	6.491	6.526	6.541	6.579	6.593	6.631

phases. In fact, along with the spinel phase, increasing amount of an orthorhombic perovskite-type structure (samples 15, 20, and to a less extent 5) plus a minor amount of corundum (sample 10), are further detected (see Table I).

(B) Unit-Cell Volume and Lattice Parameters: Lattice parameters (axes *a* and *c*), and the unit-cell volume (*V*), for the hibonite hexagonal structure along the CaNi$_x$Ti$_x$Al$_{12-2x}$O$_{19}$ join are reported in Table I. In order to visualize their evolution, compare them with literature data, and highlight possible anisotropies, those data are plotted in Fig. 2 as a function of the nominal titanium content, a common constituent of natural as well as synthetic hibonite structures.[27,30,53,54] Although in natural hibonites (mostly derived from meteoric samples), titanium is present in its reduced form (i.e., Ti^{3+}), it can be noted that a coupled substitution of Ni^{2+} + Ti^{4+} gives rise to a very similar steric effect (i.e., at octahedral site, the ionic radius of Ti^{3+} = 0.67 Å, is very close to that derived by averaging the ionic radii of Ni^{2+} and Ti^{4+} ≈ 0.65 Å).[55] An analysis of data reported in Fig. 2 reveals that:

1. The unit-cell parameters (both volume and axes) are subjected to a linear increase which is function of the degree of doping (e.g., up to a nominal content of Ni + Ti = 2 apfu, sample 10, a δV = 11.5 Å^3 is recorded). This fact is readily explained considering the difference between the ionic radii of the substituent cations. Indeed, within a same coordination site (i.e., tetrahedron, bipyramid, and octahedron), both Ni^{2+} and Ti^{4+} possess a ionic radius larger than that of the Al^{3+}.[55]

2. Up to this content of dopants (i.e., Ni + Ti = 2 apfu), Fig. 2(A) further highlights that the unit-cell volume of the investigated samples perfectly matches with that of analogous samples from literature.[27,30,53,54,56] A linear fit through our data with a nominal titanium content 0.1 ≤ x ≤ 1 apfu [dashed line between data point 1 and 10 in Fig. 2(A)], provides the following empirical relationship: V = 13.45 (14) × x_{Ti} + 586.9 (5) [R^2 = 0.96], meaning that the extrapolated volumetric value for x_{Ti} = 0 apfu is in agreement with that reported by Utsunomiya et al. for a pure calcium hexaaluminate.[56]

3. The increase in both unit-cell volume and axes, as described at point (1), is steeply interrupted for a dopants amount higher than 2 apfu (i.e., δV = 1.8 Å^3 for samples from 10 to 20). The latter is a further and clear indication that, through our synthesis conditions, high contents of nickel and titanium are not incorporated within the hibonite structure. Specifically, it can be assumed that the mechanism of the coupled substitution 2Al^{3+} = (Ni^{2+} + Ti^{4+}) is limited to a threshold value of 2 apfu.

4. Figure 2(B) also shows that, after an initial isotropic regime (i.e., *a* and *c* axes are superimposed), samples 10, 15, and 20 are characterized by an axial anisotropy (i.e., for a doping higher than 2 apfu, the hibonite structure preferentially expands along the *c*-axis). Besides to merely indicate a structural anisotropy, this preferential axial expansion could suggest a change in the mechanism of the cation incorporation into the hibonite structure (see next sections).

(D) Structural Refinements: Since nominal and recalculated composition of the hibonite phase are equivalent for a nominal content of Ni + Ti ≤ 2 apfu (see Table I), and the
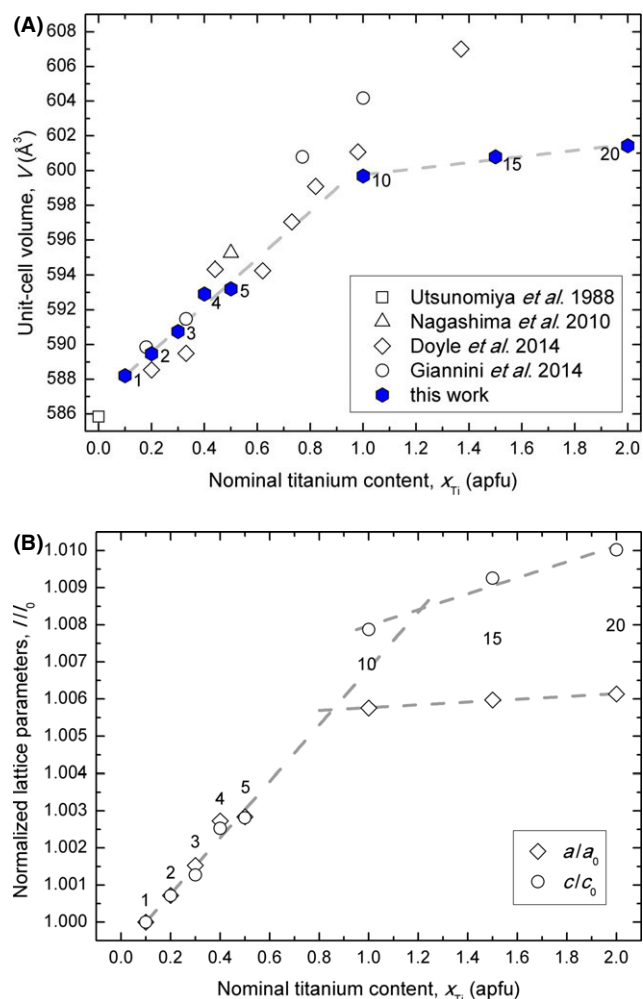
Fig. 2. Variation in the unit-cell volume (A) and lattice parameters (B) as a function of the nominal Ti content. Error bars are within the symbol size. Empty symbols in (A) refer to data from literature.

amount of associated phases is less than 10%, samples 1, 2, 3, 4, 5, and 10 are considered suitable for a comprehensive structural investigation (agreement factors and Rietveld refinement details are given in Table I). Polyhedral site occupancy and selected bond distances for samples belonging to the $CaNi_xTi_xAl_{12-2x}O_{19}$ join (with $0.1 \leq x \leq 1$) are reported in Table II.

According to what reported in the recent literature,[30,53,54] Ti^{4+} occupies both the octahedral face-sharing M4 and the trigonal bipyramidal M2 sites (Table II). Differently, no structural reports have been found on hibonite structures hosting Ni^{2+} cations. At the best of our knowledge, only one work deals with the structural features of the $LaNiAl_{11}O_{19}$ compound, a structure belonging to the magnetoplumbite group.[57] Based on the statistical distribution of nickel and aluminum ions over the five polyhedral sites of the magnetoplumbite-type structure, Laville et al.[57] reported that Ni^{2+} is mainly distributed between tetrahedral and octahedral sites of the spinel *S*-block (i.e., the correspondent M3 and M1 sites of the hibonite structure), with a preference for the tetrahedral M3. The cationic distribution of the Ni^{2+} ion in Table II partially agrees with what indicated by Laville and co-workers. In fact, for the samples here investigated, it is found that Ni^{2+} is shared between the tetrahedral M3 (the preferred one) and the octahedral face-sharing M4 site.

As well rationalized by Bermanec et al.,[27] although Ni^{2+} possesses an exceptionally large octahedral crystal field stabilization energy (CFSE), this transition-metal ion as well as other divalent cations (e.g., Zn^{2+}, Mn^{2+}, Mg^{2+}, and Fe^{2+})

shows a marked preference for the tetrahedral environment in these structural types. This fact has been related to an incorporation of the divalent cations which is electrostatically more favorable to that of more highly charged ions.[27]

Independent of changes in atomic coordinates, the unit-cell volume has been chosen to compare the mean bond distances at the polyhedral sites involved by the coupled substitution $2Al^{3+} = (Ni^{2+} + Ti^{4+})$ with those of analogous synthetic compounds taken from literature. Specifically, the metal oxygen variations at the fivefold coordinated M2 site, the tetrahedral M3 site, and the octahedral M4 site are plotted in Fig. 3 [(A C), respectively], whereas the M4 M4 interatomic distances in Fig. 4.

Besides to show a very good agreement with data from literature, Fig. 3 provides a clear indication of the incorporation of both Ni^{2+} and Ti^{4+} into the hibonite structure. Each polyhedral site undergoes an expansion proportional to the amount of the Al replaced by Ni and Ti (Fig. 3).

Furthermore, the long-range charge balance ensured by the coupled substitution $2Al^{3+} = (Ni^{2+} + Ti^{4+})$ has also a clear effect at the local scale. In fact, as clearly highlighted in Fig. 4 where samples belonging to the $CaNi_xTi_xAl_{12-2x}O_{19}$ join are compared with those possessing the same unit-cell volume, the incorporation of Ni^{2+} at the octahedral face-sharing M4 site allows a significant shortening of the M4 M4 interatomic distances. This means that the presence of octahedrally coordinated Ni^{2+} leads to a relaxation of the electrostatic repulsion due to the Ti^{4+} Ti^{4+} interactions, thus favoring an electrostatically more stable structure.

Additional indications on the relation between the cationic incorporation and the lattice strain in the hibonite structures under investigation can be inferred through *BVsum* and global instability index (*GII*) calculations (for the calculation of these parameters, readers can refer to the footnote of Table III).[58,59] As a general note, data listed in Table III well match those reported in literature.[27,30] Through the analysis of the ratio between *BVs* calculated and nominal (i.e., that deriving from the formal charges of each cation hosted in a given polyhedron), it is evident that the Ca is strongly underbonded. Specifically, the *BVs* calculated is on average lower by 27% than the nominal. This anomaly has been previously interpreted through the difference between the atomic displacement parameters of a single crystal of hibonite at low and high temperatures.[3] In the hibonite structure, Ca can be considered as a "rattling" ion (i.e., the displacement parameters show a "vibrational smearing" larger than the coordinating oxygen atoms).

Excluding the site M1, perfectly balanced, the other coordination sites are variously underbonded. Nonetheless, it is remarkable that the octahedral face-sharing M4 site exhibits calculated *BVs* that only differs by 7%, on average, from the nominal one. This further indicates that, at the local polyhedral scale, the coupled substitution $2Al^{3+} \rightarrow (Ni^{2+} + Ti^{4+})$ promotes a more electrostatically favorable environment.

Besides the *BVs* calculations, an estimation of the lattice strain (i.e., at the long scale) can be pursued by means of an evaluation of the *GII*. Values of the *GII* less than 0.05 v.u. imply unstrained structures, while values greater than ~0.2 v.u. suggest that structures become strained.[58,59]

As reported in Table III, all the hibonite structures belonging to the $CaNi_xTi_xAl_{12-2x}O_{19}$ join exhibit a lattice sparingly strained (i.e., *GII* ~ 0.3 v.u.).

(2) Optical Spectroscopy

Optical spectra are dominated by the *d–d* electronic transitions of Ni^{2+} ion, which provide three intense bands occurring at approximately 4500, 8800, and 16 000 cm^{-1}, and by the bandgap represented by the steep slope of the absorbance at high energy [Fig. 5(A)].

The main optical bands are attributed to the transitions of Ni^{2+} in tetrahedral coordination; minor bands are due to the
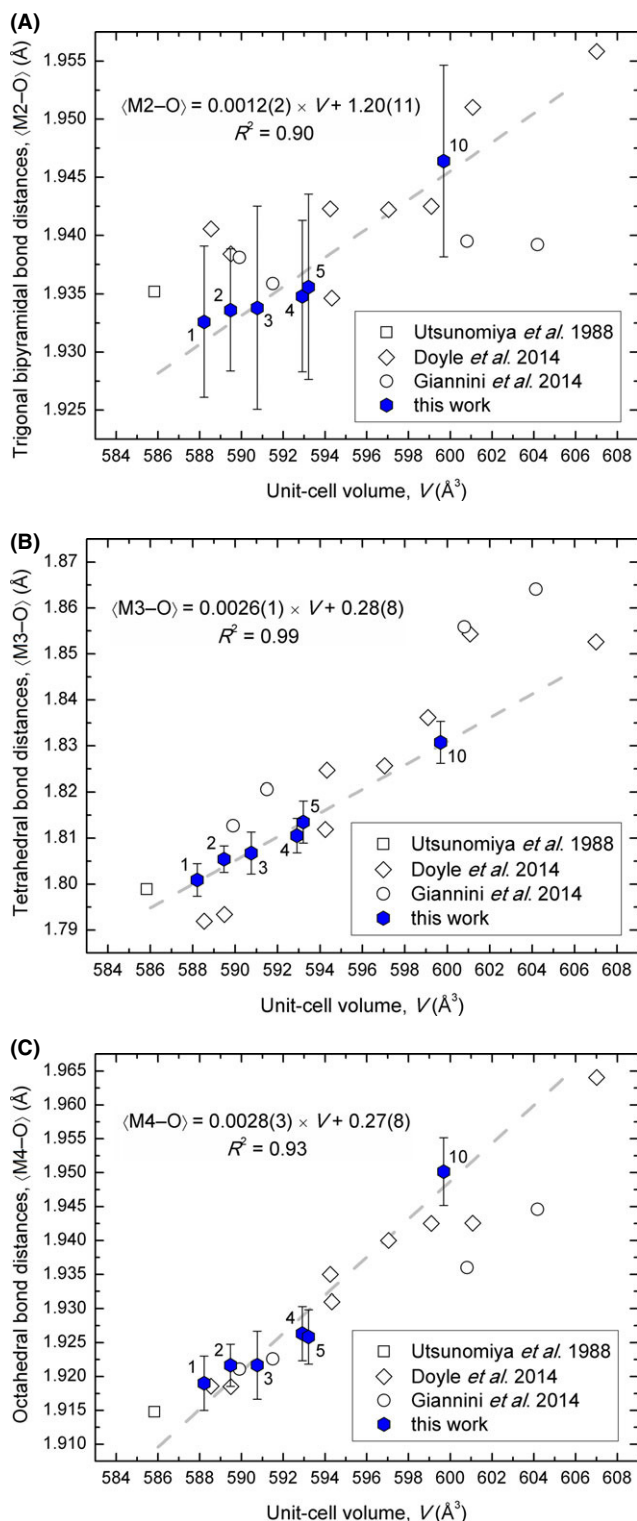
(A) $\langle M2-O \rangle = 0.0012(2) \times V + 1.20(11)$
$R^2 = 0.90$

(B) $\langle M3-O \rangle = 0.0026(1) \times V + 0.28(8)$
$R^2 = 0.99$

(C) $\langle M4-O \rangle = 0.0028(3) \times V + 0.27(8)$
$R^2 = 0.93$

Fig. 3. Variation in mean bond distances at the trigonal bipyramidal M2 site (A), tetrahedral M3 site (B), and octahedral face-sharing M4 site (C) as a function of the unit-cell volume. The equations reported in each figure, with the respective agreement factors, refer to the linear fit of the data from this study (highlighted by dashed lines). Empty symbols refer to data from literature.

transitions of Ni^{2+} in octahedral coordination. In detail, the assignment of Ni^{2+} bands was done with reference to the point symmetry, which is C_{3v} at both the M3 tetrahedron and the M4 octahedron [Table IV and Fig. 5(B)].

The possible occurrence of further chromophore ions (i.e., Ni^{3+}, Ti^{3+}) was appraised and ruled out (or considered below the detection limit of electron absorption spectroscopy) since all bands were successfully attributed to
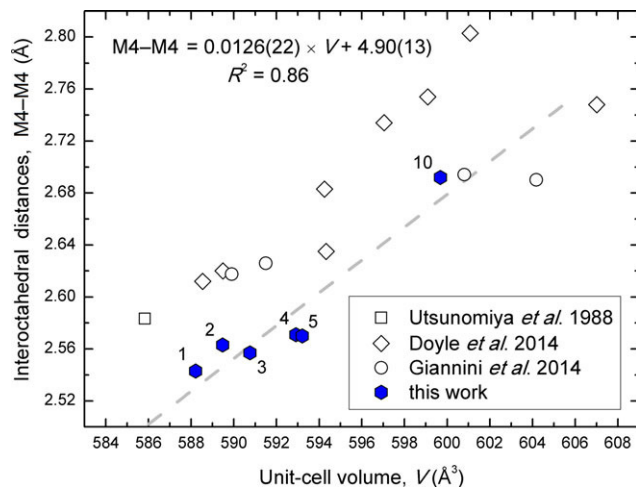

$M4-M4 = 0.0126(22) \times V + 4.90(13)$
$R^2 = 0.86$

Fig. 4. Variation in the interatomic distances M4 M4 as a function of the unit-cell volume. The equation refers to the linear fit of the data from this study (highlighted by dashed lines). Error bars are within the symbol size. Empty symbols refer to data from literature.

Ni^{2+} with good correspondence to the Tanabe–Sugano diagrams for d^8 (octahedral coordination) and d^2 (tetrahedral coordination) ions. The presence of Ni^{2+} at the fivefold coordinated site M2 or at the octahedral sites M1 and M5 was ruled out on the basis of X-ray diffraction data and crystal chemical considerations.[27,28,57] The optical reference for trivalent nickel can be the $LaAlO_3$ perovskite, where Ni^{3+} replaces Al in octahedral coordination.[60,61] The Ni^{3+} spectral features consist of two intense transitions: $^4T_{2g}$, threefold split at approximately 20 000, 24 000, and 29 000 cm^{-1}, and $^4T_{1g}$ occurring at ~10 000 cm^{-1}. This latter band has energy close to that of the $^3T_{2g}$ transition of Ni^{2+} in octahedral coordination, but no band was detected at ~20 000 cm^{-1}, even with the increasing of the $^3T_{2g}$ peak area (so ruling out the occurrence of Ni^{3+} in significant amounts). The optical spectrum of Ti^{3+}, known to occur at the M4 site of hibonite,[53] is characterized by a very broad band at ~14 000 cm^{-1} with a FWHM as high as 4000 5000 cm^{-1}.[29,62] Although the energy is nearly the same of the $^3T_{1g}$ transition of Ni^{2+} in octahedral coordination, this latter band has a FWHM of only ~1000 cm^{-1} (Table IV) thus not attributable to Ti^{3+}. At all events, Ti^{3+} was never detected for high oxygen fugacities,[62,63] as those in the synthesis conditions of the present study.

The bands due to spin-forbidden transitions of Ni^{2+} in tetrahedral coordination are partially overlapped with the strong bands originated by the spin-allowed $^3A_2$ and ^3E (^3P) transitions at 16 000–16 600 cm^{-1} [Fig. 5(B)]. This proximity brings about an appreciable spin-orbit mixing of states between quartet and doublet states, which causes a remarkable intensity increasing of the $^1T_2$, $^1A_1$ and $^1T_1$ (^1G) transitions.[64]

The optical bandgap is originated by metal oxygen charge transfer, which energy gradually decreases from sample 1 (36 400 cm^{-1}) to sample 20 (23 400 cm^{-1}). This trend is presumably the result of the growing contribution by the Ti–O charge transfer to the optical bandgap.

The band absorbance intensities increase along with the nickel amount, as expected, but with two distinct rates up to $x = 1$ and for higher x values. Significantly, the band absorbance of Ni^{2+} in tetrahedral coordination grows faster up to the sample 10 (nominal Ni and Ti doping = 1.0 apfu) but the increase is slower for nominal Ni dopings of 1.5 and 2.0 apfu. Conversely, the absorbance of bands by octahedrally coordinated Ni^{2+} increases slowly up to $x = 1.0$ then quickly from $x = 1.0$ to $x = 2.0$ apfu. All the optical bands of fourfold Ni^{2+}, once normalized for the peak area, follow the same trend in function of the nickel amount. The only

Table III. Bond Valence Sum (*BVsum*) and Global Instability Index (*GII*) Calculations for Hibonite Samples Along the Series CaNi$_x$Ti$_x$Al$_{12-2x}$O$_{19}$ (with $0.1 \leq x \leq 1$)[58,59]

Sample	1	2	3	4	5	10
[XII]Ca([VI]M1[IV−V]M2[IV]M3$_2$[VI]M4$_2$[VI]M5$_6$)O$_{19}$ *BVs* (v.u.)						
Ca	1.46	1.46	1.46	1.45	1.45	1.48
M1	2.96	2.95	2.91	2.94	3.00	2.85
M2	2.70 (3.01)	2.70 (3.05)	2.87 (3.15)	2.77 (3.12)	2.72 (3.10)	3.86 (3.74)
M3	2.47 (2.96)	2.45 (2.93)	2.45 (2.90)	2.44 (2.87)	2.44 (2.81)	2.37 (2.69)
M4	2.76 (3.03)	2.80 (3.05)	2.80 (3.02)	2.87 (3.07)	2.96 (3.14)	2.75 (2.94)
M5	2.81	2.80	2.78	2.77	2.76	2.75
O1	2.01	2.00	2.01	2.00	1.99	2.21
O2	1.70	1.69	1.71	1.68	1.68	1.80
O3	1.67	1.67	1.70	1.70	1.72	1.84
O4	1.83	1.84	1.84	1.84	1.85	1.83
O5	1.82	1.82	1.81	1.80	1.82	1.79
GII (v.u.)						
	0.32	0.32	0.30	0.31	0.30	0.25

BVs has been calculated as: $s_{ij} = \exp[(R_0 - R_{ij})/B]$, where s_{ij} is the bond valence, R_{ij} the experimental cation–anion bond length, R_0 the characteristic bond valance parameter for the cation–anion pair, and B an empirical parameter with a constant value of 0.37.[58] *GII*, defined as the root mean square of the bond valence sum deviations for all the atoms present in the asymmetric unit,[59] compares the calculated bond valences and the formal valence (V_i) for all the species (N), suggesting the degree of structural strain by means of: $GII = \sqrt{\sum_{i=1}^{N}\left[\left(\sum_j s_{ij} - V_i\right)^2 \cdot N^{-1}\right]}$.

Formal charges for Ca, M1, M5, and O are 2.00, 3.00, 3.00 and 2.00 v.u., respectively. Those of M2, M3, and M4 sites are reported within parentheses alongside of calculated values.
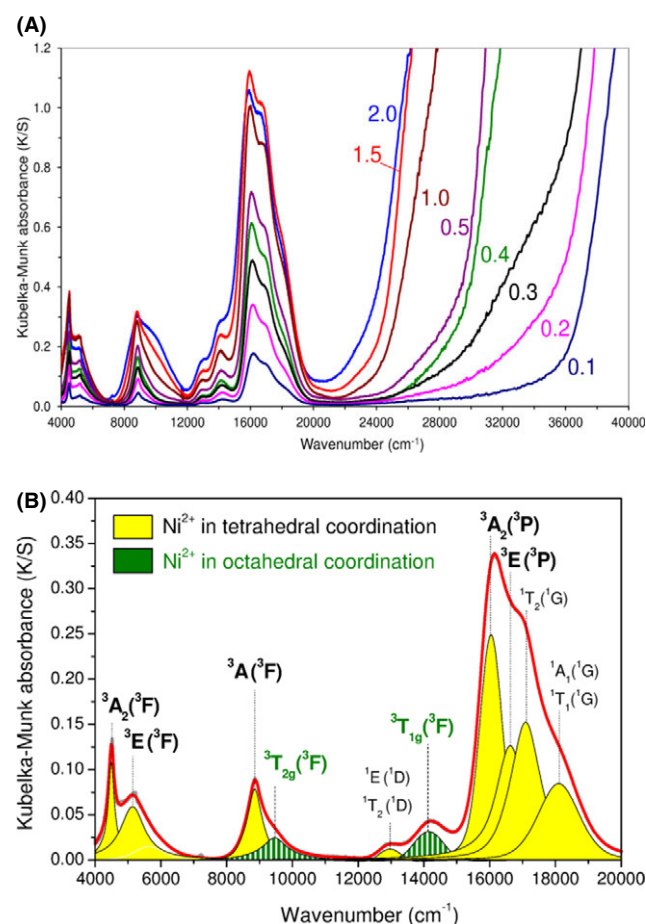
Fig. 5. Optical spectra of CaNi$_x$Ti$_x$Al$_{12-2x}$O$_{19}$ hibonites with 18 $0.1 < x < 2.0$ (A). Attribution of optical bands to *d–d* electronic transitions of tetrahedrally coordinated and octahedrally coordinated Ni^{2+}, taking sample 2 as example; spin-allowed transitions are in bold (B).

exception is represented by the fluctuating intensity of the weak band at ~13 000 cm^{-1}, attributed to the spin-forbidden transitions ^{1}E and ^{1}T$_2$ (^{1}D), which might be affected by a larger error.

The relative abundance of Ni^{2+} in tetrahedral coordination and in octahedral coordination, as determined by the ^{3}A and ^{3}T$_{2g}$ optical bands, is compared with that obtained for the M3 tetrahedron and the M4 octahedron, respectively, through Rietveld refinement of XRPD patterns (see Fig. 6). Although the employed experimental techniques (DRS and XRPD) are independent and the derived data were processed separately, Fig. 6 highlights with an appreciable degree of confidence (see the coefficient of determination R^2 derived by the linear regressions of data in Fig. 6) an excellent data agreement.

In terms of optical parameters, the crystal field strength of Ni^{2+} in tetrahedral coordination is gradually decreasing while the nominal amount of Ni is increased to $x = 1$ [Fig. 7(A)]. Although the trend is not linear, a clear tendency is appreciable, implying an elongation of the local mean Ni–O distance. This is coherent with the volume increasing from AlO$_4$ to NiO$_4$ tetrahedra (being the ionic radii of fourfold coordinated Al^{3+} and Ni^{2+} 0.39 Å and 0.55 Å,[55] respectively). The crystal field strength of Ni^{2+} in octahedral coordination is continuously decreasing for nominal Ni amounts growing up to $x = 0.4$ [Fig. 7(B)] in a way consistent with the degree of Ni–Al substitution. However, for higher Ni amounts the variation in $10Dq_{oct}$ remains within the experimental error. This trend suggests an elongation of the local mean Ni–O distance, expected because the sixfold coordinated Ni^{2+} (0.69 Å) is larger than Al^{3+} (0.535 Å), until a Ni occupancy at the site M4 close to 0.16 apfu.

Such trends are substantially confirmed considering the actual occupancy at the M3 and M4 sites instead of the nominal amount of Ni. The reason why any further incorporation of Ni is not reflected by an increasing of the $10Dq_{oct}$ has to be related also with the relatively large variation in the covalency of the Ni–O bonding at site M4, as indicated by the Racah B trend [Fig. 7(B)].

Crystal field strength values of hibonite for the tetrahedral coordination (4290–4370 cm^{-1}) are higher than NiCr$_2$O$_4$ spinel ($10Dq_{tet}$ = 4150 cm^{-1}) and (Zn,Ni)O zincite ($10Dq_{tet}$ = 4050 cm^{-1})[65] implying that the local Ni–O distance at the M3 site is shorter than in spinel and zincite tetrahedra (~1.966 and ~1.978 Å, respectively). For the octahedral coordination, the hibonite $10Dq_{oct}$ values (9430–9490 cm^{-1}) are higher than both NiO bunsenite ($10Dq_{oct}$ = 8760 cm^{-1}) and Ni$_2$SiO$_4$ liebenbergite ($10Dq_{tet}$ = 9000 cm^{-1})[66] for which

Table IV. Optical Properties of Ni²⁺ in Tetrahedral Coordination (^[IV]Ni²⁺) and Octahedral Coordination (^[VI]Ni²⁺) in Hibonites

^[IV]Ni²⁺	^[VI]Ni²⁺	1			2			3			4		
		Peak	FWHM	Area	Peak	FWHM	Area	Peak	FWHM	Area	Peak	FWHM	Area
³A₂(³F)		**4496**	**186**	**16**	**4496**	**216**	**29**	**4492**	**243**	**46**	**4488**	**262**	**57**
³E(³F)		**5124**	**640**	**12**	**5031**	**664**	**28**	**5059**	**658**	**35**	**5108**	**738**	**59**
³A(³F)		**8869**	**535**	**24**	**8854**	**551**	**52**	**8842**	**565**	**72**	**8834**	**560**	**88**
	³T₂(³F)	**9488**	**816**	**10**	**9469**	**874**	**23**	**9451**	**952**	**40**	**9431**	**960**	**59**
¹E+¹T₂(¹D)		*12 980*	*650*	*5*	*12 963*	*637*	*11*	*12 955*	*622*	*6*	*12 943*	*608*	*6*
	³T₁(³F)	**14 206**	**1052**	**13**	**14 182**	**1082**	**31**	**14 141**	**1064**	**57**	**14 117**	**1019**	**70**
³A₂(³P)		**16 073**	**809**	**109**	**16 019**	**809**	**220**	**15 982**	**833**	**338**	**15 958**	**777**	**395**
³E(³P)		**16 599**	**1152**	**93**	**16 568**	**1255**	**186**	**16 526**	**1196**	**269**	**16 449**	**1004**	**310**
¹T₂(¹G)		*17 058*	*1067*	*109*	*17 095*	*1313*	*217*	*17 096*	*1171*	*274*	*16 996*	*1092*	*409*
¹A₁+¹T₁(¹G)		*17 985*	*1578*	*73*	*18 190*	*1461*	*137*	*18 111*	*1510*	*230*	*18 078*	*1459*	*281*
MOCT		36 380			35 820			34 770			29 040		

^[IV]Ni²⁺	^[VI]Ni²⁺	5			10			15			20		
		Peak	FWHM	Area	Peak	FWHM	Area	Peak	FWHM	Area	Peak	FWHM	Area
³A₂(³F)		**4487**	**271**	**64**	**4482**	**339**	**110**	**4485**	**338**	**108**	**4487**	**268**	**62**
³E(³F)		**5124**	**779**	**83**	**5079**	**580**	**72**	**5063**	**540**	**54**	**5092**	**579**	**56**
³A(³F)		**8830**	**627**	**131**	**8776**	**672**	**177**	**8768**	**949**	**289**	**8687**	**1191**	**212**
	³T₂(³F)	**9462**	**892**	**46**	**9431**	**1110**	**125**	**9714**	**1312**	**145**	**9855**	**1960**	**385**
¹E+¹T₂(¹D)		*12 949*	*568*	*19*	*12 881*	*648*	*19*	*12 934*	*647*	*45*	*12 952*	*693*	*20*
	³T₁(³F)	**14 125**	**1024**	**86**	**14 076**	**1070**	**163**	**14 053**	**1080**	**237**	**14 049**	**1151**	**262**
³A₂(³P)		**15 930**	**855**	**491**	**15 854**	**790**	**508**	**15 810**	**1021**	**830**	**15 694**	**1230**	**909**
³E(³P)		**16 362**	**1188**	**403**	**16 332**	**1642**	**821**	**16 359**	**1862**	**751**	**16 241**	**1403**	**658**
¹T₂(¹G)		*17 023*	*1128*	*434*	*16 957*	*1282*	*617*	*16 923*	*1408*	*670*	*16 897*	*1160*	*730*
¹A₁+¹T₁(¹G)		*18 068*	*1539*	*379*	*18 136*	*1555*	*581*	*18 171*	*1622*	*740*	*17 957*	*1646*	*616*
MOCT		29 230			24 690			24 170			23 420		

*In samples 15 and 20 there is a significant contribution from Ni²⁺ in NiAl₂O₄.

*The energy (peak, cm⁻¹), full width at half maximum (FWHM, cm⁻¹), and intensity (peak area, arbitrary units) are listed for absorption bands due to spin-allowed transitions (bold) and spin-forbidden transitions (italic) along with the metal–oxygen charge-transfer (MOCT) bandgap energy (cm⁻¹).
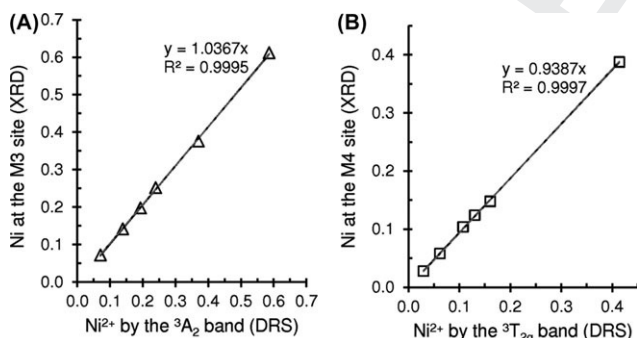
Fig. 6. Relative abundance of tetrahedrally coordinated Ni²⁺ (by DRS) versus Ni occupancy at the M3 site, by XRD (A). The same for octahedrally coordinated Ni²⁺ versus Ni occupancy at the M4 site (B).

Ni–O distance is ~2.08 Å. These crystal field strength data support for local Ni–O bond distances much longer than the corresponding Al–O distances in the undoped hibonite. Such a circumstance implies a remarkable structural relaxation around Ni²⁺, particularly in tetrahedral coordination, where a supposed $\langle Ni-O\rangle_{local} \sim 1.94$ Å is much longer than the mean M3–O distance (1.80 Å, Table II). Analogously, the supposed $\langle Ni-O\rangle_{local} \sim 1.97$ Å in octahedral coordination is longer than the mean M4–O distance (1.91 Å, Table II).

The Racah B values were found to be between 810 and 820 cm⁻¹ for Ni²⁺ in tetrahedral coordination. These values are slightly higher than Ni-doped zincite, 795 cm⁻¹.[65] The Racah B values for Ni²⁺ in octahedral coordination vary over a wider range: from 815 to 860 cm⁻¹, which is comprised between the values known for bunsenite and liebenber-

gite: 808–878 cm⁻¹, respectively.[66] The diminishing trends suggest, for both Ni²⁺ in tetrahedral and octahedral coordination, a more covalent Ni–O bonding by increasing the nominal amount of Ni. Although apparently in contrast with the elongation of the Ni–O bond distances, the enhanced covalent character of the Ni–O bonds with the Ni amount can be actually ascribed to differences between the ionic-covalent parameter of Ni²⁺ with respect to those of Al³⁺ and Ti⁴⁺ ions.[67]

The color of Ni–Ti codoped hibonite stems from the very strong ³A₂ + ³E (³P) bands of Ni²⁺ in tetrahedral coordination, which absorb almost completely the yellow to orange wavelengths of the visible spectrum. As a consequence, a window of transmitted light is left in the blue and green region [Fig. 5(A)], hence the perceived turquoise color.[34] This peculiar color is achieved because of the high crystal field strength of Ni²⁺ in hibonite, which implies a shift of its ³A₂ + ³E (³P) bands toward higher energy (from red to orange-yellow wavelengths, so the resulting color turns blue-green instead of the typical green of many Ni²⁺-bearing oxides).

(3) Dopant Partition

Proportionally to the difference in ionic radii, the Ni and Ti replacement for Al cations into the hibonite structure induces a regular increase in the unit-cell parameters up to a doping amount of 2 apfu. As a matter of fact, below this threshold, hibonite retains its oxygen stoichiometry, since such a replacement occurs according to a paired Ni²⁺ + Ti⁴⁺ → 2Al³⁺ substitution. When dopants are added at nominal contents from 2 to 4 apfu, hibonite is found in equilibrium with an increasing amount of secondary phases, mainly NiAl₂O₄ spinel and CaTiO₃ perovskite. In these conditions, hibonite is able to accommodate the doping ions up to about 3.7 apfu
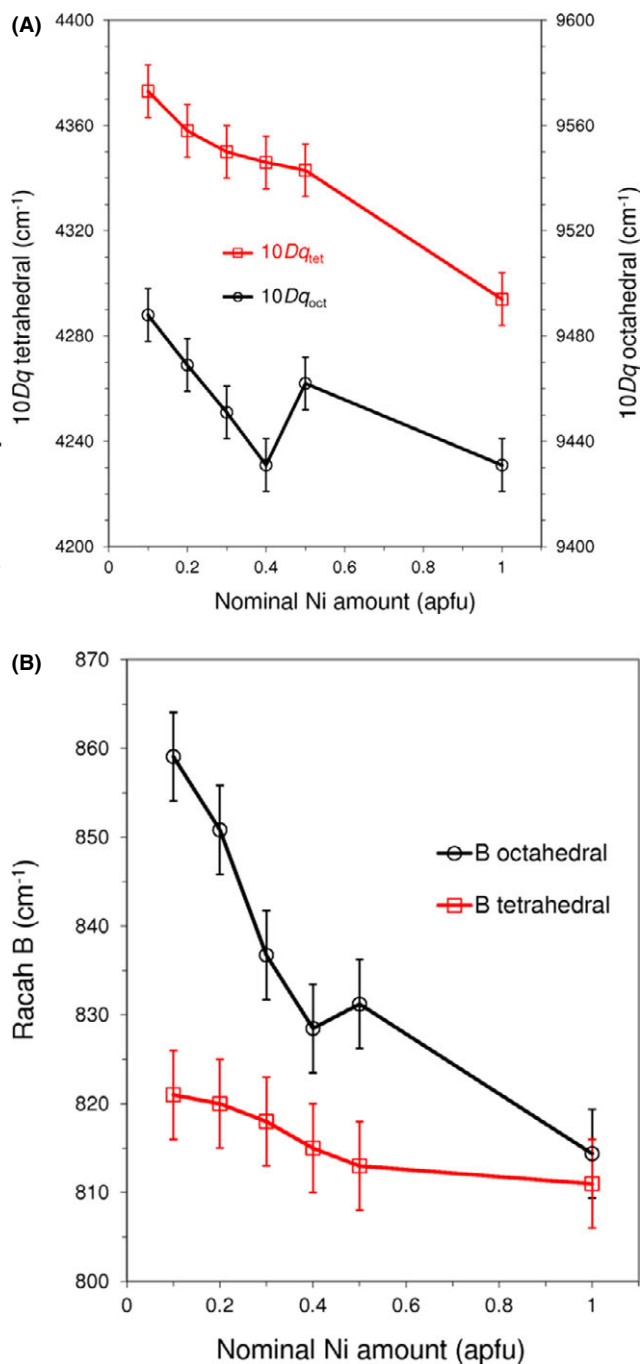
Fig. 7. Crystal field strength (A) and Racah *B* parameter (B) of **19** Ni^{2+} in tetrahedral and octahedral coordination.

(Ni+Ti). On the other hand, with doping over 2 apfu, Ni^{2+} and Ti^{4+} are no longer incorporated in the same molar concentrations. Such a circumstance implying a nonstoichiometry of the hibonite structure.

About the doping partition between the Al-centered polyhedra of the hibonite lattice, it has been observed a marked preference of Ni^{2+} for the smallest tetrahedral site M3 and of Ti^{4+} for the largest pentacoordinated site M2. Predictions based on crystal field stabilization energy (CFSE) are not matched, since the Ni^{2+} ion should prefer the octahedral coordination, according to its large CFSE (on average -137 ± 2 kJ/g·ion in the M4 site of hibonite) that is about the double of Ni^{2+} at the tetrahedral site M3 (average CFSE -65 ± 1 kJ/g·ion). The observed preferential accommodation of Ni^{2+} and Ti^{4+} ions in the hibonite crystal structure does not depend on merely steric reasons stemming from the much longer ionic radii of dopants with respect to Al^{3+}. Considerations related to the *BVsum* at the

tetrahedral site M3 provide converging indications, namely the *BVsum* at the M3 site for synthetic $CaAl_{12}O_{19}$ compound is 2.5 v.u.[56] Therefore, this nearly regular tetrahedral site (point symmetry C_{3v}) is so constrained by the structural features (i.e., layers of approximately closest-packed oxygen atoms) that it always results as underbonded. As a consequence, a preferential ordering of divalent species (e.g., Zn^{2+}, Mn^{2+}, Mg^{2+}, Ni^{2+}, Fe^{2+}) often occurs in natural specimens as well as synthetic compounds.[24,25,27,29,30,57] In agreement with Burns and Burns,[29] the entry of divalent cations larger than the Al^{3+} at the tetrahedral site M3 could relieve the structural strain as it happens in the β-alumina structure.[29,68] The observed M3–O and **10** M4–O mean distances, shorter than those expected on the averaged variation of ionic radii from Al^{3+} to (Al and Ni) at M3 and to (Al, Ni, and Ti) at M4 sites, entail a certain structural relaxation to accommodate Ni^{2+} (and Ti^{4+}) in a "compressed" status. Such a relaxation is responsible for the high crystal field strength value mentioned above, which in turn leads to a blue-shift of the absorbance bands.

IV. Conclusions

X-ray powder diffraction and electronic absorption spectroscopy experimental techniques have been employed to investigate eight samples of hibonite pigments (with nominal stoichiometry $CaAl_{12\,2x}Ni_xTi_xO_{19}$, where *x*: 0.1, 0.2, 0.3, 0.4, 0.5, 1.0, 1.5, and 2.0 apfu) obtained through combustion synthesis. Fully accommodated within the hibonite crystal structure up to approximately $x = 1$ apfu, Ni^{2+} and Ti^{4+} ions have been found to be shared between the tetrahedral M3 and the octahedral M4 sites, the former, and between the bipyramidal M2 and the octahedral M4 sites, the latter.

A marked agreement between diffraction and optical data unequivocally ratifies the cationic partition of both Ni and Ti ions. In terms of optical parameters, Ni^{2+} is found to be preferentially incorporated in tetrahedral coordination, up to 0.3 apfu at the M3 site, and at the M4 octahedron as well (up to 0.19 apfu).

The crystal field strength of fourfold coordinated Ni^{2+} regularly decrease, implying an elongation of the local Ni–O bond distances that is consistent with the volume increasing from AlO_4 to NiO_4 tetrahedra registered by diffraction data.

In conclusion, it has been found that in the case of hibonite structure, the main $^3A_2$ and ^3E (^3P) transitions absorb more in the blue and less in the green, with respect to other Ni^{2+} compounds having lower $10Dq$ values. Thus, the color of the investigated samples results to be a greenish-blue, close to cyan or turquoise.

Supporting Information

Additional Supporting Information may be found in the online version of this article:

Table SI. Chemical Formula and Metal Molar Ratios Used in Sample Design and Preparation

References

[1]M. Dondi and R. A. Eppler, *Ceramic Colorants. Ullmann's Encyclopedia of Industrial Chemistry*; pp. 1–18. Wiley-VCH, Weinheim, Germany, 2014.
[2]K. Nassau, *The Physics and Chemistry of Color: The Fifteen Causes of Color*, 2nd Edition. Wiley-VCH, Weinheim, Germany, 2001.
[3]R. G. Burns, *Mineralogical Applications of Crystal Field Theory*, 2nd Edition. Cambridge University Press, Cambridge, U.K., 1993.
[4]M. Wildner, M. Andrut, and C. Rudowicz, "Optical Absorption Spectroscopy in Geosciences. Part I: Basic Concepts of Crystal Field Theory" Chapter 3 in *Spectroscopic Methods in Mineralogy*, Vol. **6**, Edited by A. Beran

and E. Libowitzky. EMU Notes in Mineralogy, Eötvös University Press, Budapest, Hungary, 2004.

[5]A. Escardino, S. Mestre, A. Barba, V. Beltrán, and A. Blasco, "Synthesis Mechanism of an Iron–Chromium Ceramic Pigment," *J. Am. Ceram. Soc.*, **83** [1] 29–32 (2000).

[6]F. Bondioli, A. M. Ferrari, C. Leonelli, T. Manfredini, L. Linati, and P. Mustarelli, "Reaction Mechanism in Alumina/Chromia (Al_2O_3–Cr_2O_3) Solid Solutions Obtained by Coprecipitation," *J. Am. Ceram. Soc.*, **83** [8] 2036–40 (2000).

[7]F. Matteucci, G. Cruciani, M. Dondi, and M. Raimondo, "The Role of Counterions (Mo, Nb, Sb, W) in Cr-, Mn-, Ni- and V-Doped Rutile Ceramic Pigments. Part 1. Crystal Structure and Phase Transformations," *Ceram. Int.*, **32** [4] 385–92 (2006).

[8]M. Dondi, G. Cruciani, G. Guarini, F. Matteucci, and M. Raimondo, "The Role of Counterions (Mo, Nb, Sb, W) in Cr-, Mn-, Ni- and V-Doped Rutile Ceramic Pigments. Part 2. Colour and Technological Properties," *Ceram. Int.*, **32** [4] 393–405 (2006).

[9]G. Cruciani, et al., "Structural Relaxation Around Cr^{3+} in $YAlO_3$-$YCrO_3$ Perovskites From Electron Absorption Spectra," *J. Chem. Phys. A*, **113** [49] 13772–8 (2009).

[10]A. García, R. Galindo, C. Gargori, S. Cerro, M. Llusar, and G. Monrós, "Ceramic Pigments Based on Chromium Doped Alkaline Earth Titanates," *Ceram. Int.*, **39** [4] 4125–32 (2013).

[11]M. Ocaña, A. Caballero, A. R. González-Elí, P. Tartaj, and C. J. Serna, "Valence and Localization of Praseodymium in Pr-Doped Zircon," *J. Solid State Chem.*, **139** [2] 412–5 (1998).

[12]S. Ardizzone, G. Cappelletti, P. Fermo, C. Oliva, M. Scavini, and F. Scime, "Structural and Spectroscopic Investigations of Blue, Vanadium-Doped $ZrSiO_4$ Pigments Prepared by a Sol-Gel Route," *J. Phys. Chem. B*, **109** [47] 22112–9 (2005).

[13]R. Gieré, C. T. Williams, and G. R. Lumpkin, "Chemical Characteristics of Natural Zirconolite," *Schweiz. Miner. Petrogr.*, **78** [3] 433–59 (1998).

[14]R. W. Cheary and A. A. Coelho, "A Site Occupancy Analysis of Zirconolite $CaZr_xTi_{3-x}O_7$," *Phys. Chem. Miner.*, **24** [6] 447–54 (1997).

[15]A. S. Pakhomova, S. V. Krivovichev, S. V. Yudintsev, and S. V. Stefanovsky, "Synthetic Murataite-3C, a Complex Form for Long-Term Immobilization of Nuclear Waste: Crystal Structure and Its Comparison With Natural Analogues," *Z. Kristallog*, **228** [3] 151–6 (2013).

[16]N. P. Laverov, S. V. Yudintsev, S. V. Stefanovsky, B. I. Omel'yanenko, and B. S. Nikonov, "Murataite as a Universal Matrix for Immobilization of Actinides," *Geol. Ore Deposit+*, **48** [5] 335–56 (2006).

[17]J. Carda, G. Monros, P. Escribano, and J. Alarcon, "Synthesis of Uvarovite Garnet," *J. Am. Ceram. Soc.*, **72** [1] 160–2 (1989).

[18]J. Carda, G. Monros, V. Esteve, and J. M. Amigo, "Cation Distribution by Powder X-Ray Diffraction in Uvarovite-Grossularite Garnets Solid Solutions Synthesized by the Sol-Gel Method," *J. Solid State Chem.*, **108** [1] 24–8 (1994).

[19]G. Cruciani, M. Dondi, T. Stoyanova, F. Matteucci, J. Carda, and A. L. Costa, "Malayaite Ceramic Pigments: A Combined Optical Spectroscopy and Neutron/X-ray Diffraction Study," *Mater. Res. Bull.*, **44** [8] 1778–85 (2009b).

[20]E. Lopez-Navarrete, A. Caballero, V. M. Orera, F. J. Lázaro, and M. Ocana, "Oxidation State and Localization of Chromium Ions in Cr-Doped Cassiterite and Cr-Doped Malayaite," *Acta Mater.*, **51** [8] 2371–81 (2003).

[21]M. M. Hirschmann and M. S. Ghiorso, "Activities of Nickel, Cobalt, and Manganese Silicates in Magmatic Liquids and Applications to Olivine/Liquid and to Silicate/Metal Partitioning," *Geochim. Cosmochim. Acta*, **58** [19] 4109–26 (1994).

[22]C. J. Capobianco and A. A. Amelin, "Metal-Silicate Partitioning of Nickel and Cobalt: The Influence of Temperature and Oxygen Fugacity," *Geochim. Cosmochim. Acta*, **58** [1] 125–40 (1994).

[23]V. K. Singh and K. K. Sharma, "Low-Temperature Synthesis of Calcium Hexa-Aluminate," *J. Am. Ceram. Soc.*, **85** [4] 769–72 (2002).

[24]D. Holtstman, R. Norrestam, and A. Sjodin, "Plumboferrite: New Mineralogical Data and Atomic Arrangement," *Am. Mineral.*, **80** [9–10] 1065–972 (1995).

[25]H. Graetsch and W. Gebert, "Cation Distribution in Magnetoplumbite Type $SrTi_6Co_6O_{19}$," *Z. Kristallog.*, **210** [1] 9–13 (1995).

[26]K. Kato and H. Saalfeld, "Verfeinerung der Kristallstruktur von $CaO·6Al_2O_3$," *Neues Jahrb. Mineral. Abh.*, **109** 192–200 (1968).

[27]V. Bermanec, D. Holtstam, D. Sturman, A. J. Criddle, M. E. Back, and S. Šćavničar, "Nežilovite, a New Member of the Magnetoplumbite Group, and the Crystal Chemistry of Magnetoplumbite and Hibonite," *Can. Mineral.*, **34** [6] 1287–97 (1996).

[28]A. M. Hofmaister, B. Wopenka, and A. J. Locock, "Spectroscopy and Structure of Hibonite, Grossite and $CaAl_2O_4$: Implication for Astronomical Environments," *Geochim. Cosmochim. Acta*, **68** [21] 4485–503 (2004).

[29]R. G. Burns and V. M. Burns, "Crystal Chemistry of Meteoritic Hibonites," *J. Geophys. Res.*, **89** [S1] C313–21 (1984).

[30]M. Nagashima, T. Armbruster, and T. Hainschwang, "A Temperature-Dependent Structure Study of Gem-Quality Hibonite From Myanmar," *Mineral. Mag.*, **74** [5] 871–85 (2010).

[31]M. Dondi, M. Ardit, G. Cruciani, and C. Zanelli, "Tetrahedrally Coordinated Co^{2+} in Oxides and Silicates: Effect of Local Environment on Optical Properties," *Am. Mineral.*, **99** [8–9] 1736–45 (2014).

[32]M. Ardit, M. Dondi, C. Zanelli, and G. Cruciani, "Structural Relaxation Around Cr3 + at the Na(Al1-XCrx)P2O7 Octahedral Site: A XRPD and EAS Study," *Z. Kristallog.*, **229** [10] 687–97 (2014).

[33]M. Ardit, G. Cruciani, M. Dondi, and C. Zanelli, "Pigments Based on Perovskite"; pp. ???–??? Chapter 14 in *Perovskites and Related Mixed Oxides,*

Vol. **???**, Edited by P. Granger, V. I. Parvulescu, S. Kaliaguine and W. Prellier. Wiley-VCH, Weinheim, Germany, ???. (In press)

[34]G. Costa, M. J. Ribeiro, J. A. Labrincha, M. Dondi, F. Matteucci, and G. Cruciani, "Ni-Doped Hibonite ($CaAl_{12}O_{19}$): A New Turquoise Blue Ceramic Pigment," *J. Eur. Ceram. Soc.*, **29** [13] 2671–8 (2009).

[35]A. Leite, G. Costa, W. Hajjaji, M. J. Ribeiro, M. P. Seabra, and J. A. Labrincha, "Blue Cobalt Doped-Hibonite Pigments Prepared From Industrial Sludges: Formulation and Characterization," *Dyes Pigm.*, **81** [3] 211–7 (2009).

[36]R. Ianoş, I. Lazău, C. Păcurariu, and P. Barvinschi, "Fuel Mixture Approach for Solution Combustion Synthesis of $Ca_3Al_2O_6$ Powders," *Cement Concrete Res.*, **39** [7] 566–72 (2009).

[37]R. Ianoş, I. Lazău, C. Păcurariu, and P. Barvinschi, "Peculiarities of $CaO·6Al_2O_3$ Formation by Using Low-Temperature Combustion Synthesis," *Eur. J. Inorg. Chem.*, **2008** [6] 925–30 (2008a).

[38]R. Ianoş and P. Barvinschi, "Solution Combustion Synthesis of Calcium Zirconate, $CaZrO_3$, Powders," *J. Solid State Chem.*, **183** [3] 491–6 (2010).

[39]I. Lazau, C. Pacurariu, Z. Ecsedi, and R. Ianos,*Unconventional Methods Used for Oxide Compounds Synthesis*. Ed. Politehnica, Timisoara, Romania, 2006.

[40]I. Lazau, C. Pacurariu, and R. Ianos, *Oxide Compounds Synthesis*. Ed. Politehnica, Timisoara, Romania, 2008.

[41]R. Ianoş, I. Lazău, C. Păcurariu, and P. Barvinschi, "Solution Combustion Synthesis of $MgAl_2O_4$ Using Fuel Mixtures," *Mater. Res. Bull.*, **43** [12] 3408–15 (2008b).

[42]I. Lazău, R. Ianoş, C. Păcurariu, and C. Savii, "Spinel Preparation by Combustion Synthesis. The Influence of Synthesis Conditions on the Features of the Resulted Spinel $MgAl_2O_4$ Powder," *Romanian J. Mater.*, **38** [3] 224–32 (2008).

[43]R. Ianos, I. Lazau, C. Pacurariu, and P. Barvinschi, "The Synthesis of Tricalcium Aluminate, $3CaO×Al_2O_3$, Using Low-Temperature Combustion Synthesis"; pp. 361–7 in Proceedings of 10th ECERS Conference, ???, Berlin, Germany, 2007.

[44]E. Leal, A. C. F. de Melo Casto, N. L. de Freita, H. De Lucena Lira, R. H. G. A. kiminami, L. Gama, "$NiAl_2O_4$ Catalysts Prepared by Combustion Reaction Using Glycine as Fuel," *Mater. Res. Bull.*, **46** [9] 1409–13 (2011).

[45]A. C. Larson and R. B. Von Dreele, "*GSAS, General Structure Analysis System*"; pp. 86–748. Los Alamos National Laboratory, Los Alamos, NM, 1988.

[46]B. H. Toby, "EXPGUI, A Graphical User Interface for GSAS," *J. Appl. Crystallogr.*, **34** [2] 210–3 (2001).

[47]H. S. C. O'Neill, W. A. Dollase, and C. R. Ross, "Temperature Dependence of the Cation Distribution in Nickel Aluminate ($NiAl_2O_4$) Spinel: A Powder XRD Study," *Phys. Chem. Minerals*, **18** [5] 302–19 (1991).

[48]S. Sasaki, C. T. Prewitt, and J. D. Bass, "Orthorhombic Perovskite $CaTiO_3$ and $CdTiO_3$: Structure and Space Group," *Acta Crystallogr. C*, **43** [9] 1668–74 (1987).

[49]V. L. Cherginets, V. N. Baumer, S. S. Galkin, L. V. Glushkova, T. P. Rebrova, and Z. V. Shtitelman, "Solubility of Al_2O_3 in Some Chloride-Fluoride Melts," *Inorg. Chem.*, **45** [18] 7367–71 (2006).

[50]A. Marfunin, *Physics of Minerals and Inorganic Materials: An Introduction*. Springer-Verlag, Berlin, Germany, 1979.

[51]Y. Tanabe and S. Sugano, "On the Absorption Spectra of Complex Ions. I," *J. Phys. Soc. Jpn.*, **9** [5] 753–66 (1954).

[52]M. Andrut, M. Wildner, and C. Rudowicz, "Optical Absorption Spectroscopy in Geosciences. Part II: Quantitative Aspects of Crystal Fields"; pp. ???–???, Chapter 4 in *Spectroscopic Methods in Mineralogy*, Vol. **6**, Edited by A. Beran and E. Libowitzky. EMU Notes in Mineralogy, Eötvös University Press, Budapest, Hungary, 2004.

[53]P. M. Doyle, P. F. Schofield, A. J. Berry, A. M. Walker, and K. S. Knight, "Substitution of Ti^{3+} and Ti^{4+} in Hibonite ($CaAl_{12}O_{19}$)," *Am. Mineral.*, **99** [7] 1369–82 (2014).

[54]M. Giannini, T. Boffa Ballaran, and F. Langenhorst, "Crystal Chemistry of Synthetic Ti-Mg-Bearing Hibonites: A Single-Crystal X-ray Study," *Am. Mineral.*, **99** [10] 2060–7 (2014).

[55]R. Shannon, "Revised Effective Ionic Radii and Systematic Studies of Interatomic Distances in Halides and Chalcogenides," *Acta Crystallogr. A*, **32** [5] 751–67 (1976).

[56]A. Utsunomiya, K. Tanaka, H. Morikawa, F. Marumo, and H. Kojima, "Structure Refinement of $CaO 6Al_2O_3$," *J. Solid State Chem.*, **75** [1] 197–200 (1988).

[57]F. Laville, M. Perrin, A. M. Lejus, M. Gasperin, R. Moncorge, and D. Vivien, "Synthesis, Crystal Growth, Structural Determination, and Optical Absorption Spectroscopy of the Magnetoplumbite Type Compound $LaNiAl_{11}O_{19}$," *J. Solid State Chem.*, **65** [3] 301–8 (1986).

[58]I. D. Brown, *The Chemical Bond in Inorganic Chemistry.. The Bond Valence Model*. Vol. **12**, IUCr Monograph on Crystallography, Oxford University Press, New York, 2002.

[59]A. Salinas-Sanchez, J. L. Garcia-Muñoz, J. Rodriguez-Carvajal, R. Saez-Puche, and J. L. Martinez, "Structural Characterization of R_2BaCuO_5 (R = Y, Lu, Yb, Tm, Er, Ho, Dy, Gd, Eu and Sm) Oxides by X-Ray and Neutron Diffraction," *J. Solid State Chem.*, **100** [2] 201–11 (1992).

[60]M. N. Sanz-Ortiz, F. Rodríguez, A. Baranov, and G. Demazeau, "Synthesis Under Pressure and Characterizations Through Optical Spectroscopy of Jahn-Teller Cations (LS Ni^{3+}, IS Co^{3+}) as Probes Diluted in a Perovskite Matrix," *J. Phys.: Conf. Series*, **121** [9] 092003 (2008).

[61]M. N. Sanz-Ortiz, F. Rodríguez, J. Rodríguez, and G. Demazeau, "Optical and Magnetic Characterisation of Co^{3+} and Ni^{3+} in $LaAlO_3$: Interplay Between the Spin State and Jahn–Teller Effect," *J. Phys.-Conden. Mat.*, **23** [41] 415501 (2011).

[62]P. D. Ihinger and E. Stolper, "The Color of Meteoritic Hibonite: An Indicator of Oxygen Fugacity," *Earth Planet. Sci. Lett.*, **78** [1] 67–79 (1986).

[63]J. R. Beckett, D. Live, F. D. Tsay, L. Grossman, and E. Stolper, "Ti 3 + in Meteoritic and Synthetic Hibonite," *Geochim. Cosmochim. Acta*, **52** [6] 1479–95 (1988).

[64]H. A. Weakliem, "Optical Spectra of Ni^{2+}, Co^{2+}, and Cu^{2+} in Tetrahedral Sites in Crystals," *J. Chem. Phys*, **36** [8] 2117–40 (1962).

[65]R. Pappalardo, D. L. Wood, and R. C. Linares Jr, "Optical Absorption Study of Ni-Doped Oxide Systems. I," *J. Phys. Chem.*, **35** [4] 1460–78 (1961).

[66]D. Reinen, "Kationenverteilung zweiwertiger $3d^n$-Ionen in oxidischen Spinell-, Granat-und anderen Strukturen"; pp. 114–154 in *Structure and bonding*, Vol. **???**, Edited by C. K. Jorgensen, J. B. Neilands, R. S. Nyholm, D. Reinen and R. J. P. Williams. Springer-Verlag, Berlin, Germany, 1970.

[67]G. R. Rossman, "Optical Spectroscopy"; pp. 207–54 in *Spectroscopic Methods in References Mineralogy and Geology*, Vol. **18**, Edited by F. C. Hawthorne. Reviews in Mineralogy Series. Mineralogical Society of America, Washington, DC, 1988.

[68]K. Momma and F. Izumi, "VESTA 3 for Three-Dimensional Visualization of Crystal, Volumetric and Morphology Data," *J. Applied Crystallogr.*, **44** [6] 1272–6 (2011).

[69]M. Lenglet, "Iono-Covalent Character of the Metal–Oxygen Bonds in Oxides: A Comparison of Experimental and Theoretical Data," *Act. Passive Electron. Compon.*, **27** [1] 1–60 (2004).

[70]J. M. Newsam and B. C. Tofield, "Non-Stoichiometry in Beta Aluminas," *Solid State Ionics*, **5**, 59–64 (1981).   □

16